

*Improving the Uniformity of Revolver Designs for the National Ignition Facility*

**Yujia Yang**

Brighton High School

Rochester, New York

Advisor: Dr. R. S. Craxton

**Laboratory for Laser Energetics**

University of Rochester

Rochester, New York

November 2017

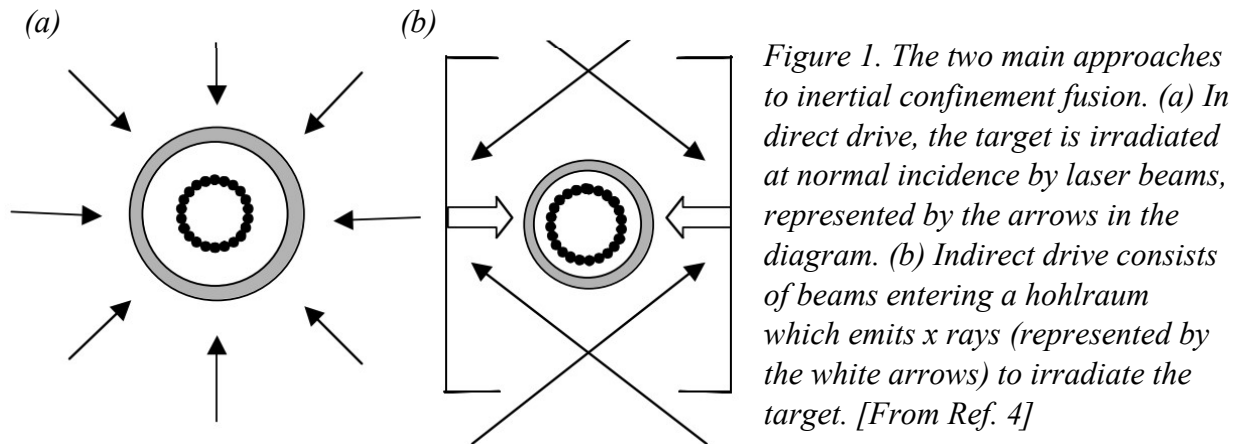
## 1. Abstract

The proposed *Revolver* target, consisting of nested beryllium, copper, and gold shells, is an alternative model, with approximately twice the radius, to the conventional target for implosions on the National Ignition Facility (NIF). A new design has been developed for *Revolver* using custom phase plates, since the maximum allowed defocus of current NIF phase plates produces focal spots that are too small, leading to significant nonuniformity in the azimuthal direction. This work considered variations of the size and ellipticity of the beams and their intensity profiles and pointings. The flux limiter was shown to have little effect on the uniformity of various designs, showing that the heat flow in *Revolver* is predominantly classical. The new design, developed using the 2D hydrodynamics simulation code *SAGE*, optimizes the NIF beam parameters to decrease the overall nonuniformity by a factor of 1.25 and to reduce the azimuthal nonuniformity by more than two-fold.

## 2. Introduction

Fusion is a nuclear reaction in which the nuclei of hydrogen isotopes, typically deuterium (1 neutron) and tritium (2 neutrons), combine to form a helium nucleus, releasing a high-energy neutron in the process. This reaction can be achieved by using laser beams to irradiate a target capsule containing these two isotopes of hydrogen, ablating the outer layer outwards, while an equal and opposite force compresses the deuterium and tritium (DT) inwards. Targets used for designs on the National Ignition Facility (NIF) at Lawrence Livermore National Laboratory are thin plastic (CH) shells, approximately 1.5 mm in radius, filled with DT in solid, liquid, or gaseous form. The lasers are able to bring the DT to conditions of extremely high temperature, density, and pressure, overpowering the Coulombic repulsion forces of positively charged nuclei to allow fusion reactions to occur for a short period of time. If the product of the compressed fuel's density and radius is large enough, the helium nuclei will deposit their energy in the fuel in an event known as ignition. If ignition occurs, the energy produced from the fusion reactions may equal the energy input, a phenomenon known as breakeven. Once high energy gain is achieved, when the energy output is approximately a hundred times the energy input, laser fusion can be considered an abundant alternative energy source.

There are currently two approaches to laser fusion: direct drive<sup>1,2</sup> and indirect drive.<sup>3</sup> Direct drive is illustrated by Figure 1(a), where laser beams directly irradiate the target from normal incidence at all angles. The University of Rochester's Laboratory for Laser Energetics currently uses this configuration on the OMEGA laser system to conduct their fusion experiments.



The other approach is indirect drive [Figure 1(b)], where the target lies inside a cylindrical hohlraum, made of a material with a high atomic number (typically gold). The lasers are aimed through two holes at the top and bottom of the hohlraum. When beams hit the hohlraum, it emits x rays that provide the energy needed to compress the target capsule. Though approximately 80% of the laser's initial energy is absorbed and given off as x rays, the target only absorbs about 20% of the energy, the rest being absorbed by the gold or escaping through the holes of the hohlraum. Despite this loss of energy, its efficiency is comparable to direct drive as indirect drive allows for greater uniformity through the x ray radiation. Though NIF is designed for indirect drive, it's currently carrying out both direct and indirect drive fusion experiments.

Since NIF's current configuration is set up for indirect drive, its beam ports aren't in the ideal locations for direct drive. There are a total of 48 laser beam ports, located in four rings in each hemisphere at angles  $\theta$  of  $23.5^\circ$ ,  $30.0^\circ$ ,  $44.5^\circ$ , and  $50.0^\circ$  from the vertical. Laser beams are arranged in groups of four, called a quad, and each port contains one quad. If NIF's beams with their current configuration are all pointed towards the center of the target, the equator is extremely underdriven in comparison to the poles, resulting in an ellipsoidal shape rather than a sphere, as illustrated by Figure 2(a). As a result, a method with repointings of beams, called polar

direct drive,<sup>5</sup> is used to obtain uniform direct drive implosions on NIF [Figure 2(b)]. In polar direct drive, the beams are repositioned towards the equator in order to drive the equator the same amount as the poles.

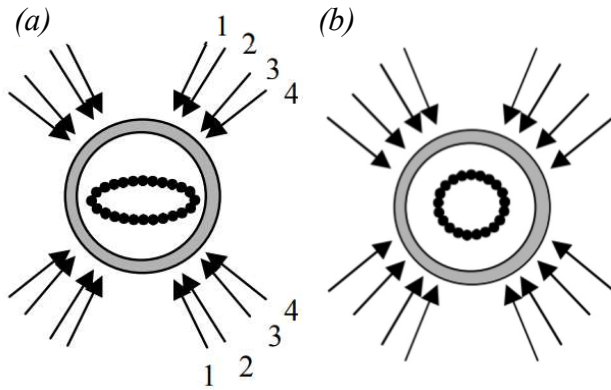


Figure 2. Two ways in which NIF's beam configuration for indirect drive can compress a target through direct drive. (a) When laser beams are aimed at the target's center, the poles compress much more compared to the equator. Rings 1-4 are indicated. (b) Repositioning beams to be pointed closer to the equator results in a nearly uniform implosion. [From Ref. 4]

A new, alternative design has been proposed for experiments on the NIF, shown in Figure 3, which displays a comparison of the standard target<sup>2</sup> [Figure 3(a)] to *Revolver*<sup>6</sup> [Figure 3(b)]. *Revolver* is twice as large in diameter compared to the standard target, 6 mm to the standard 3 mm. It is claimed that its size and the properties of its materials make it a low risk, lower reward alternative to the high risk, high reward setup of the standard target.

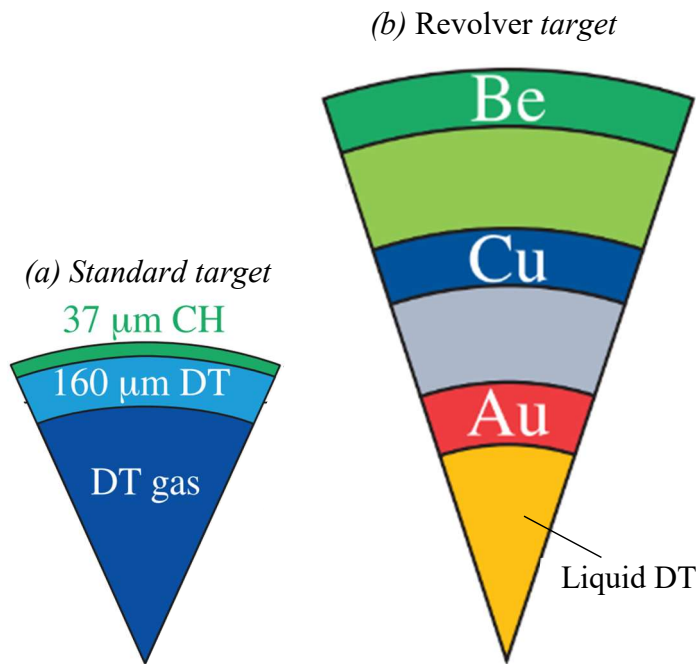


Figure 3. Comparison between the standard target and *Revolver*. (a) The standard target consists of deuterium-tritium gas surrounded by solid DT, contained in a plastic shell. (b) *Revolver* is approximately twice the diameter of the standard target, consisting of nested gold, copper, and beryllium shells. [(a) from Ref. 2, (b) from Ref. 6]

While the standard target consists of gaseous DT in the center, surrounded by a layer of DT ice and a thin layer of plastic (CH), *Revolver* consists of nested gold, copper, and beryllium shells, with liquid DT inside the gold shell and low-density foam inside the beryllium and copper shells.

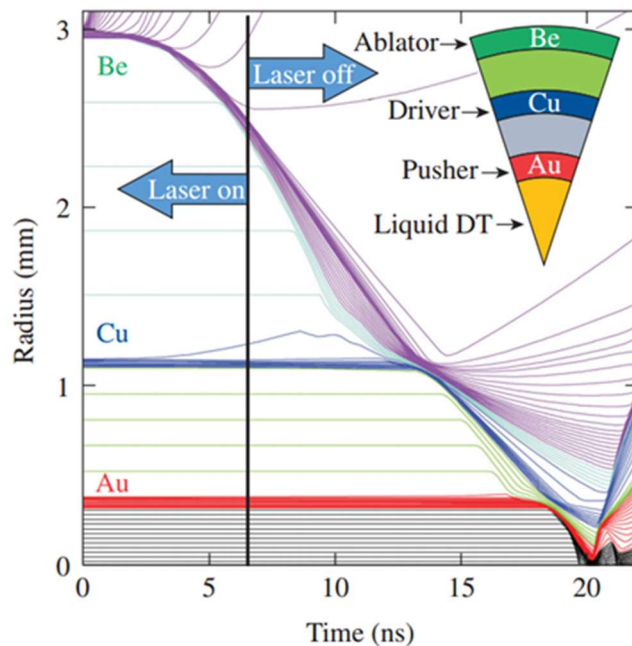


Figure 4. Radius vs. time graph of the Revolver target. The end of the laser pulse is shown by the black vertical line; the pulse continues for 6.7 ns before turning off. The beryllium absorbs the laser pulse energy for only a short period before imploding to hit the copper shell, which then implodes, hitting the gold shell that compresses the DT. It is claimed that refreshment of material at each successive shell reduces magnifying nonuniformity. [From Ref. 6]

Figure 4 shows the implosion path of the three shells.<sup>6</sup> The laser pulse accelerates the beryllium inwards, which implodes to hit the copper shell, which then implodes to hit the gold shell that then compresses the liquid DT for fusion reactions to occur. The gold acts as a thermal blanket, allowing much of the heat from fusion to be retained within the deuterium. In addition, gold restricts the expansion of DT as fusion reactions occur, slowing the expansion of the *Revolver* target as a whole. The duration of the laser pulse is another major difference between the two targets. In the standard target, the laser is usually kept on until the target reaches full compression. However, on *Revolver*, the laser pulse [Figure 5] is short, turning off at 6.7 ns, before the beryllium reaches the copper shell [Figure 4].

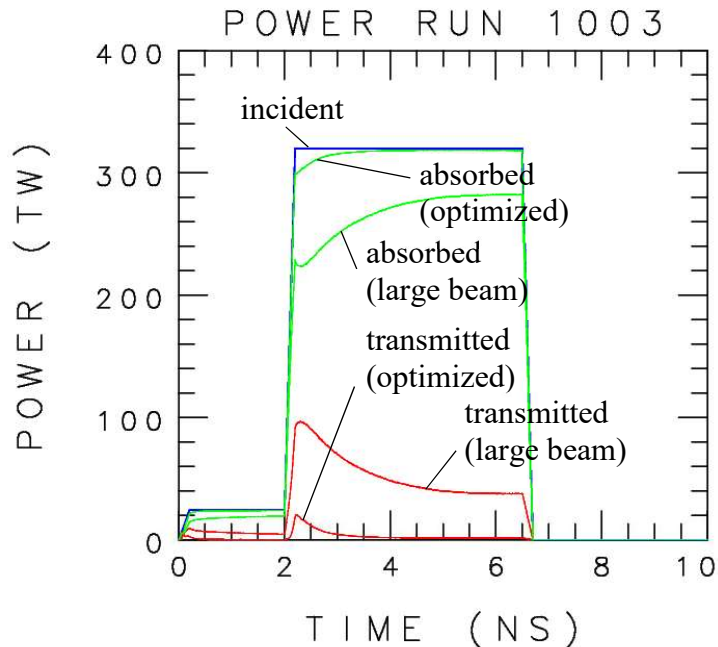


Figure 5. Power vs. time graph showing incident, absorbed, and transmitted power in terawatts. The temporal profile (incident) is shown in blue and has a step before the main laser pulse at 2 ns; the laser turns off at 6.7 ns. Green lines indicate absorbed energy and red lines show transmitted energy for two designs (see Section 6). [Runs 1003, 1284]

In a previous design<sup>7</sup> using NIF's current phase plates with a defocus of 35 mm (approximately the maximum defocus available), the beam spots were small and produced regions of localized over- and undercompression. The goal of this work was to achieve uniformity along the azimuthal direction by using larger beam spots on the target's surface to compensate for the larger size of the *Revolver* target. In order to produce larger beam spots, custom phase plates were implemented to control the size and shape of beam spots on the target surface. Through bigger spots as well as other adjustments, including pointings and ellipticity of beam spots, azimuthal nonuniformity was reduced by more than two-fold through the use of custom phase plates, while overall nonuniformity was lowered as well.

### 3. Previous Design

A raytrace of a Ring 4 beam of the design using NIF's current phase plates<sup>7</sup> is shown in Figure 6. As seen, the beam is aimed near the equator, and nearly all of the rays of this design are completely absorbed, while those that are deflected still deposit close to all of their energy in the target. Overall, the target has an extremely high energy absorption of 99.6%.

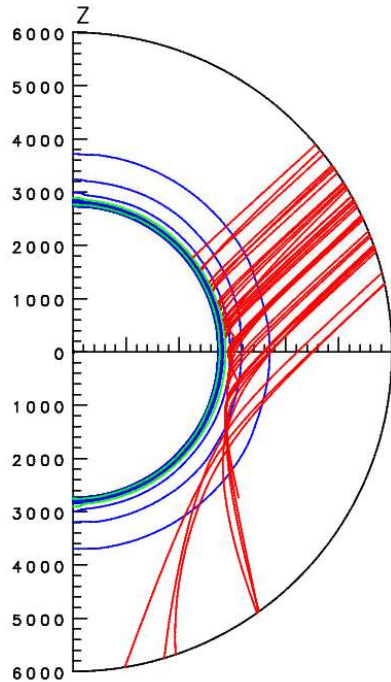


Figure 6. Raytrace of the bottom-right beam of Ring 4 at 5 ns of the design using NIF's current phase plates. All rays are aimed tightly in the vicinity of the equator. Density contours are shown by the blue circular lines, which show increasing density as the blue semicircles decrease in radius. The vertical axis on the left shows distances in  $\mu\text{m}$ . [Run 1002]

Due to this high absorption of beam energy by the equator, the equator is able to compress uniformly in relation to the poles, leading to an extremely low root-mean-square (rms) nonuniformity of 0.17% in the  $\theta$  direction,<sup>7</sup> as shown by the plot of the center-of-mass radius vs.  $\theta$  in Figure 7, which comes from a 2D calculation that averages values over the azimuthal angle  $\phi$ .

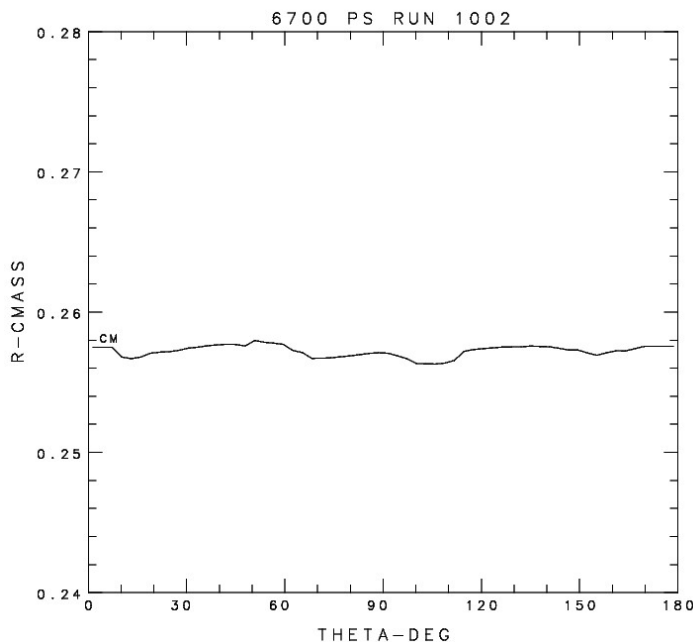


Figure 7. Center-of-mass radius (cm) vs.  $\theta$  (degrees) of the lowest nonuniformity design using NIF's current phase plates. The line is almost completely straight, showing extremely low variation along the  $\theta$  direction.

Even at maximum defocus, the current NIF beams produce small beam spots on the target,<sup>7</sup> as seen by the 3D center-of-mass contour plot in Figure 8, resulting in several localized regions of over- and undercompression. This means that despite the low nonuniformity in the  $\theta$  direction, variations along the  $\phi$  direction are too large to achieve breakeven.<sup>8</sup>

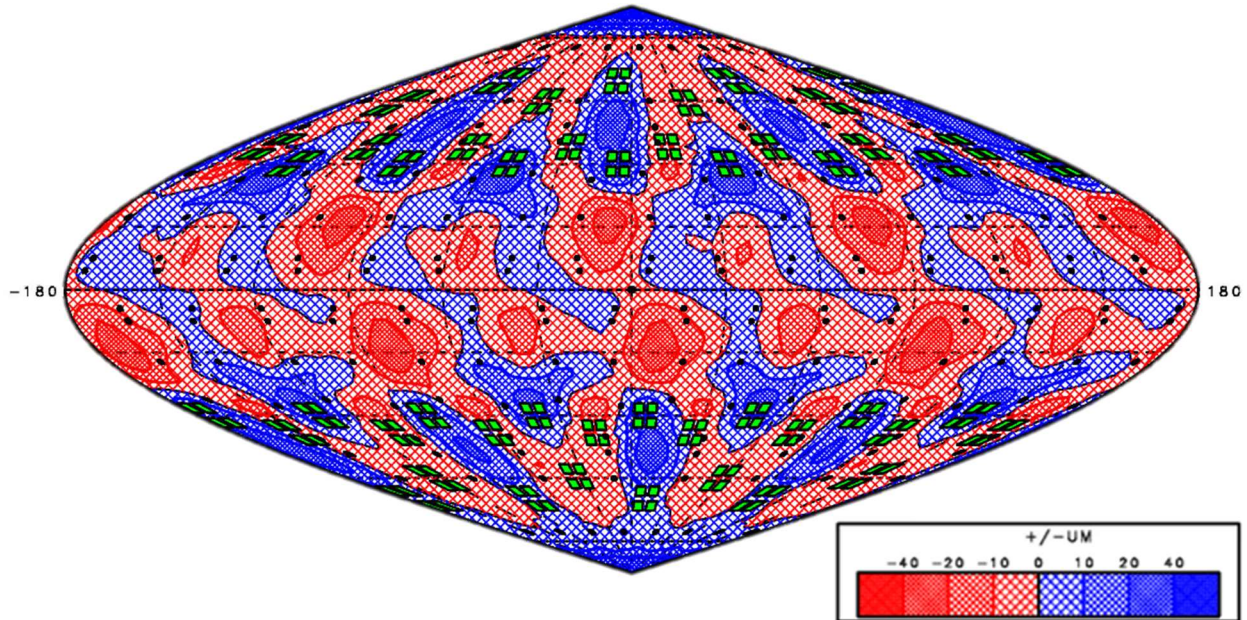


Figure 8. The 3D center-of-mass plot at 6.7 ns with contours indicating deviations from the average radius of the beryllium shell in  $\mu\text{m}$  (projection over the whole target surface). The green squares are the locations of beam ports and the black dots are the beam pointings. Blue regions indicate undercompression and red regions show overcompression. It can be seen that there are large variations along the azimuth, resulting in the  $\phi$  variation being too large to achieve breakeven. The plot was constructed as described by Tucker by combining the center-of-mass plot of Figure 7 from a 2D simulation with the 3D energy deposition.<sup>9</sup> [Run 1002]

The relationship between different elements of rms nonuniformity is given by the equation

$$rms^2 = (rms\theta)^2 + (rms\phi)^2 \quad (1)$$

where rms is the total rms nonuniformity, rms $\theta$  is the component of nonuniformity in the  $\theta$  direction, and rms $\phi$  is the component of nonuniformity in the  $\phi$  direction. The rms nonuniformity is defined as the rms of the deviations shown in Figure 8 divided by the average radius of 2580

$\mu\text{m}$ . While the design has a relatively high total nonuniformity of 0.40%, it has an exceptionally low  $\theta$  nonuniformity of 0.17%, which then makes its  $\phi$  nonuniformity comparatively high at 0.36%, according to Equation 1. Another quantity of interest is the rms of deviations shown in Figure 8 divided by the distance traveled, since this gives the rms nonuniformity of the average velocity up to the end of the laser pulse. This value is 2.6%, far over the ideal 1% needed to achieve breakeven.

#### 4. Optimized Design

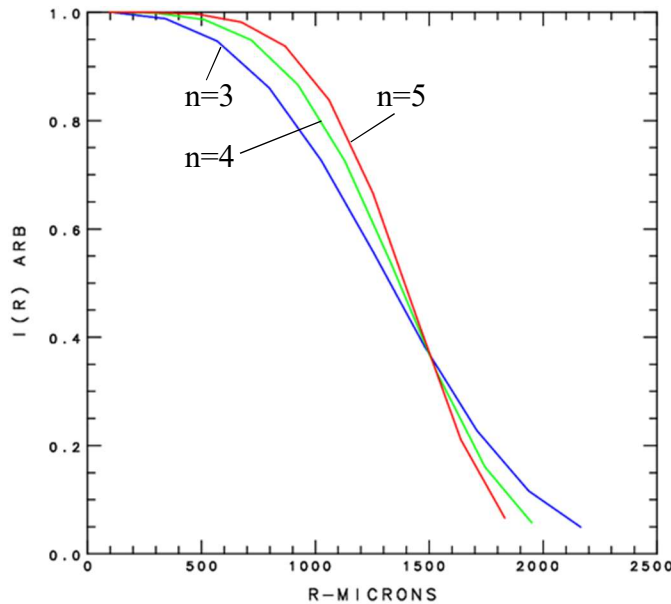
One of the main parameters considered when implementing custom phase plates was the intensity profile of each beam. Beams that were larger in the horizontal ( $\phi$ ) direction were used compared with the previous design (Section 4.1). After the beam sizes in the  $\phi$  direction were established, the ellipticity for each beam was set to decrease the beam sizes in the  $\theta$  direction to deposit energy uniformly in that direction (Section 4.2). Section 4.3 addresses slight adjustments in beam pointings in both the  $\theta$  and  $\phi$  directions to minimize nonuniformities. Parameters were varied separately to initially determine which would improve the uniformity, then several parameters were simultaneously varied in incremental changes to arrive at the new design with the lowest nonuniformity. In the optimized design, azimuthal nonuniformity was significantly reduced with total nonuniformity being lower as well (Section 4.4). It should be noted that all beams maintained identical temporal profiles throughout and their energies were not modified.

##### 4.1 Intensity Profiles

For each beam, the intensity  $I$  is given as a function of radius  $r$  by the equation

$$I(r) = I_0 \exp[-(r/r_0)^n] \quad (2)$$

where  $I_0$  is the maximum intensity in the beam spot,  $r_0$  is the radius of the beam spot, and  $n$  is the Gaussian order that determines the shape of the intensity profile within the beam. Figure 9 shows how varying  $n$  affects the intensity profile when the radius of the beam spot is  $1500\ \mu\text{m}$ .

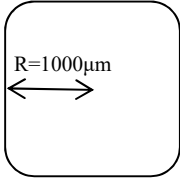
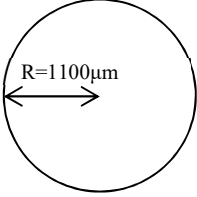
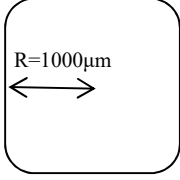
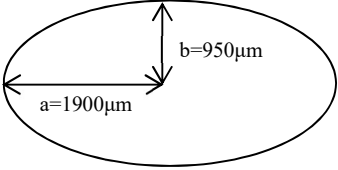
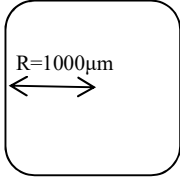
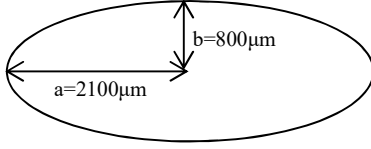


*Figure 9. Graph of intensity of laser beam as a function of radius. The greatest intensity is at  $r=0$  and it falls off as  $r$  increases. The variable that determines this falloff rate is  $n$ ; as  $n$  increases, the intensity profile becomes steeper. The blue, green, and red lines represent  $n=3$ ,  $n=4$ , and  $n=5$ , respectively for an  $r_0$  value of  $1500\ \mu\text{m}$ .*

In the optimized design, beams in rings 1 and 2 had  $r_0=1100\ \mu\text{m}$  and  $n=3$ . In both rings 3 and 4,  $n$  was also set to be 3, but the ring 3 quads had  $r_0$  set to  $1900\ \mu\text{m}$  while the  $r_0$  of ring 4 beams was  $2100\ \mu\text{m}$ .

## 4.2 Ellipticity

Table 1 shows the shape of the focal spots on target in the optimized design as opposed to the previous design. Using NIF's current phase plates, the largest focal spot that can be obtained is approximately  $1000\ \mu\text{m}$  in radius and takes the shape of a square with rounded corners, the shape and size that's set for all four rings. With custom phase plates, these beams can be made significantly more elliptical and larger. To obtain these elliptical beam spots on the target,  $r_0$  from the intensity profile function was set to the horizontal radius of the ellipse, and a separate parameter set the ellipticity of each ring, which multiplied the  $r_0$  to obtain the vertical radius.

	Previous Design	Optimized Design
Rings 1, 2		
Ring 3		
Ring 4		

*Table 1: Parameters of size and ellipticity in all rings for the previous and optimized designs. All beams in the optimized design increased in size. Beams of Ring 3 became a 2:1 ellipse with a radius of 1900  $\mu\text{m}$  along the horizontal axis. Ring 4 beams became even more elliptical with a horizontal radius of 2100  $\mu\text{m}$  and a vertical radius of 800  $\mu\text{m}$ .*

In rings 1 and 2, the optimized design's beams deviate very little from the previous design, the beams being only slightly larger, 1100  $\mu\text{m}$  in radius to the previous 1000  $\mu\text{m}$ , and more circular. In rings 3 and 4, the beam shapes of the optimized design contrast greatly to the previous design. The ring 3 beams are 2:1 ellipses with a radius of 1900  $\mu\text{m}$  along the greater axis, nearly twice that of the previous 1000  $\mu\text{m}$ . The ring 4 beams have an even greater ellipticity and are 2100  $\mu\text{m}$  in radius along their greater axis, more than twice the length of the previous design.

Figure 10 depicts the energy deposition plots of the bottom-right beam of each quad in Ring 4 of the previous design [Figure 10(a)] as compared to the optimized design [Figure 10(b)]. It is evident that even when the energy deposition of only one beam in each quad is shown, the uniformity of energy deposition along the ring where the beams are pointed is greater in the optimized design.

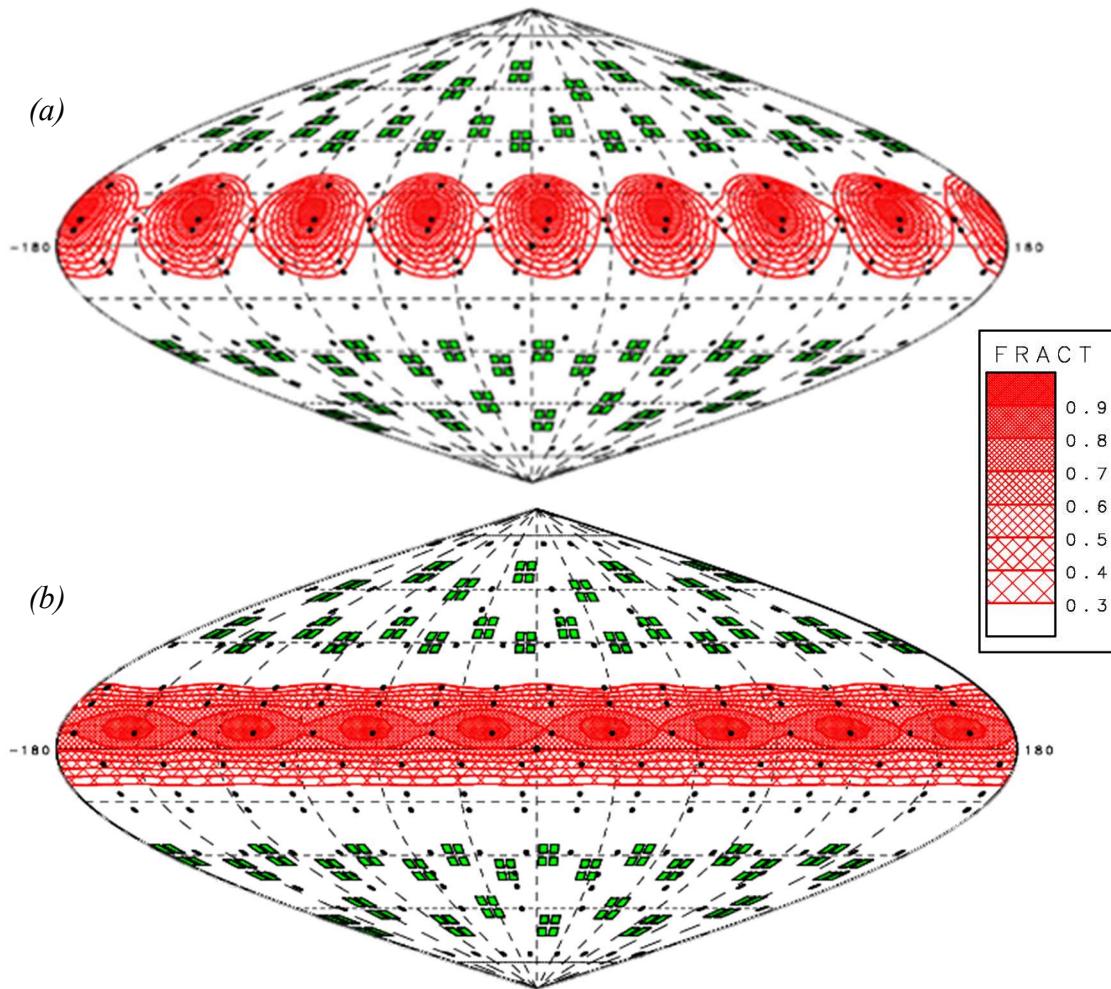


Figure 10. Energy deposition plots of the bottom-right beams of Ring 4 with contours showing fraction of maximum. (a) In the previous design using NIF's phase plates at maximum defocus, small beam spots are produced, depositing energy in eight distinct locations around the azimuth. (b) With bigger beam spots in the optimized design, the pattern becomes much less distinct and a more uniform band of energy appears around the azimuth. [Runs 1002, 1284]

When the energy deposition plots of all beams of ring 4 quads are compared between the two designs [Figure 11], the increase in uniformity is further emphasized. Whereas in the previous design, across the ring 4 beams, there is an eight-fold pattern of spots of greater energy deposition than the rest of the target, the optimized design has an almost completely uniform band of deposited energy across the target's surface, which makes the pattern nearly imperceptible.

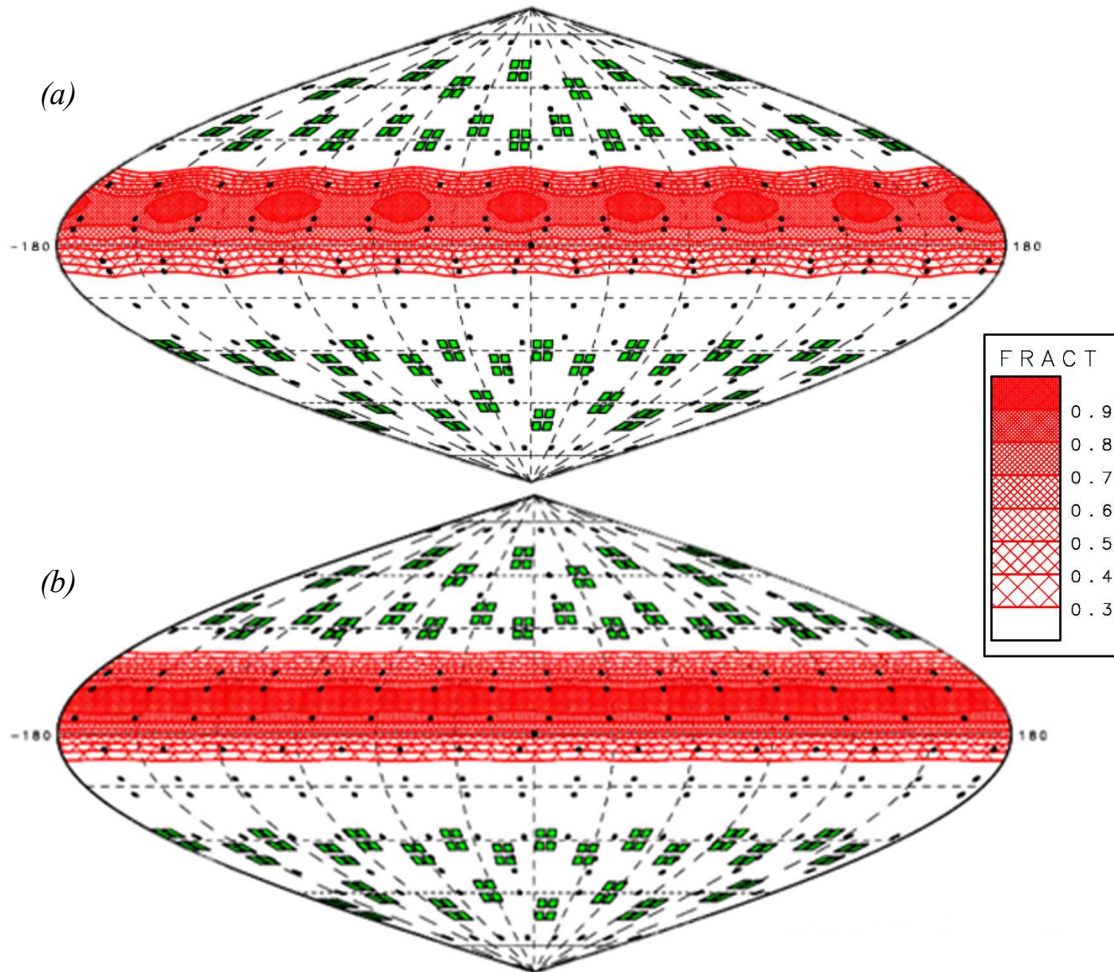


Figure 11. As Figure 10, but energy deposition plots of all beams of Ring 4 combined. (a) In the previous design, an eightfold pattern is still clearly visible, contributing to the localized overcompression regions on the 3D center-of-mass plot (Fig. 8). (b) In the optimized design, bigger beam spots greatly diminish nonuniformities in energy deposition. [Run 1002, 1284]

### 4.3 Pointings

Though the pointings of the optimized design do not differ drastically from the previous design, the slight modifications contribute to minimizing nonuniformity. Only pointings of Rings 3 and 4 were shifted to decrease nonuniformity. Changes in the  $\phi$  direction were almost insignificant. All angle shifts were set to either  $11.25^\circ$  or  $-11.25^\circ$  to maintain uniformly distributed energy in the  $\phi$  direction. The total  $\phi$  angle of  $360^\circ$  has to be split between the sixteen top and sixteen bottom beams in each of Rings 3 and 4, meaning they should all be positioned

22.5° from each other. Setting the right beams of each quad to 11.25° and the left beams to -11.25° ensures equal spacing. The pointings in the  $\theta$  direction were changed as shown in Table 2. In the previous design, the top and bottom beams of each quad could be closer in the  $\theta$  direction and still maintain the same energy deposition uniformity. However, with elliptical beam spots that were shorter vertically [Table 1], the top and bottom beams of each quad had to be spread further apart in the  $\theta$  direction in order to maintain uniform distribution of energy.

	Previous Pointings	Optimized Pointings
Ring 3 top beams	53°	51°
Ring 3 bottom beams	55°	67°
Ring 4 top beams	80°	73°
Ring 4 bottom beams	84°	84°

*Table 2. Pointings in Rings 3 and 4 of the previous and optimized designs in the  $\theta$  direction. The pointings in Rings 3 and 4 were spread further apart in the optimized design to compensate for the smaller vertical size of the beam spots.*

#### 4.4 Improved Azimuthal Uniformity

In the optimized design where custom phase plates are implemented, the nonuniformity in the  $\phi$  direction is drastically reduced, more than two-fold, from the design using NIF's current phase plates. Figure 12 shows the 3D center-of-mass radius plot for the optimized design, and when compared with Figure 8, it is clearly evident that the variation in the azimuthal direction has been reduced significantly. The small, localized regions of over and under-compression that were once present have been mitigated and the contours on the plot of the optimized design don't even pass the +20  $\mu\text{m}$  and -20  $\mu\text{m}$  marks (aside from small regions near the poles). In the optimized design, the total rms nonuniformity is 0.32% (a decrease of 1.25 from the previous design), the nonuniformity in the  $\theta$  direction is 0.27%, and the nonuniformity in the  $\phi$  direction is 0.17%, a major drop from the previous  $\phi$  nonuniformity of 0.36%. In addition, the average rms velocity nonuniformity is reduced from 2.6% for the previous design to 2.1% for the optimized design, of which 1.8% is in the  $\theta$  direction and 1.1% is in the  $\phi$  direction.

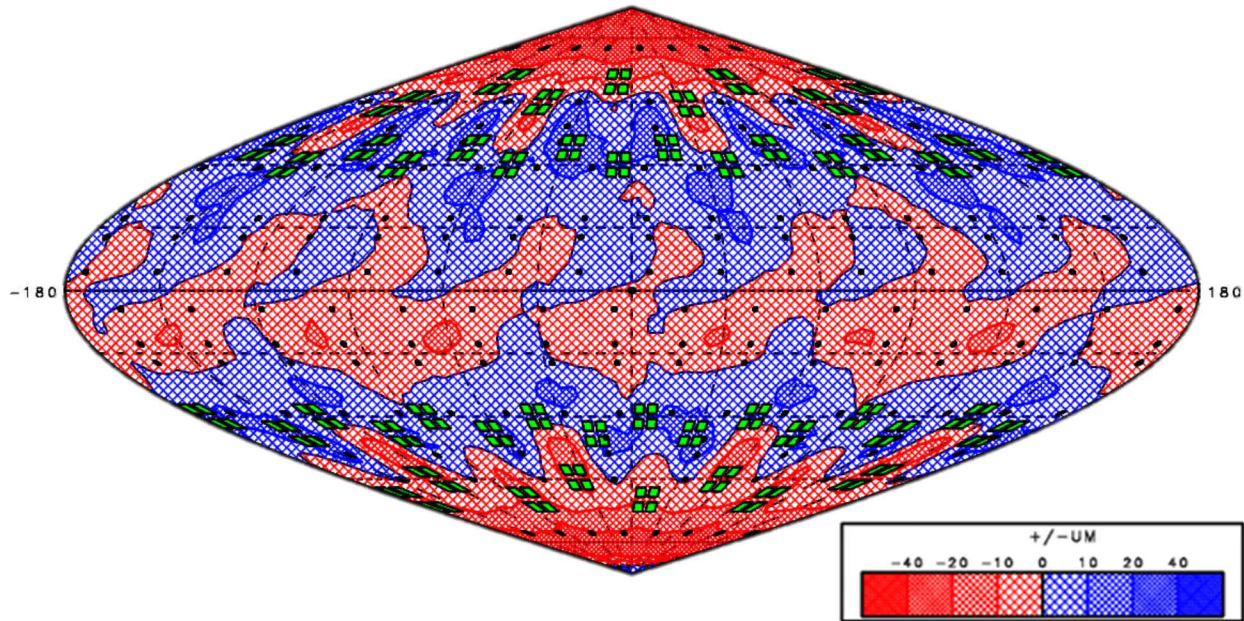


*Figure 12. 3D center-of-mass plot for the optimized design at 6.7 ns. This has a much lower nonuniformity in the azimuthal direction than the previous design. The regions of over- and undercompression are no longer localized to small regions and are spread out along the azimuth. It should be noted that all 3D center-of-mass plots share the same scale. [Run 1284]*

Plots of the energy deposition vs.  $\phi$  at  $\theta$  angles of  $60^\circ$  and  $50^\circ$  are shown in Figure 13, where red represents the design using NIF's current phase plates and blue represents the optimized design. At  $\theta=60^\circ$  [Figure 13(a)], the red line has approximately twice the variation in intensity as the blue line, similar to the total  $\phi$  variation of the previous design that is approximately twice that of the optimized design. At  $\theta=50^\circ$  [Figure 13(b)], the difference in azimuthal variation is much greater: the azimuthal variation of the previous design is nearly five times that of the optimized design. This distinctly illustrates the improvement of azimuthal uniformity in the optimized design. Despite clearly visible improvements, detailed simulations similar to those run in Reference 8 are needed to see if the optimized design will reach breakeven.

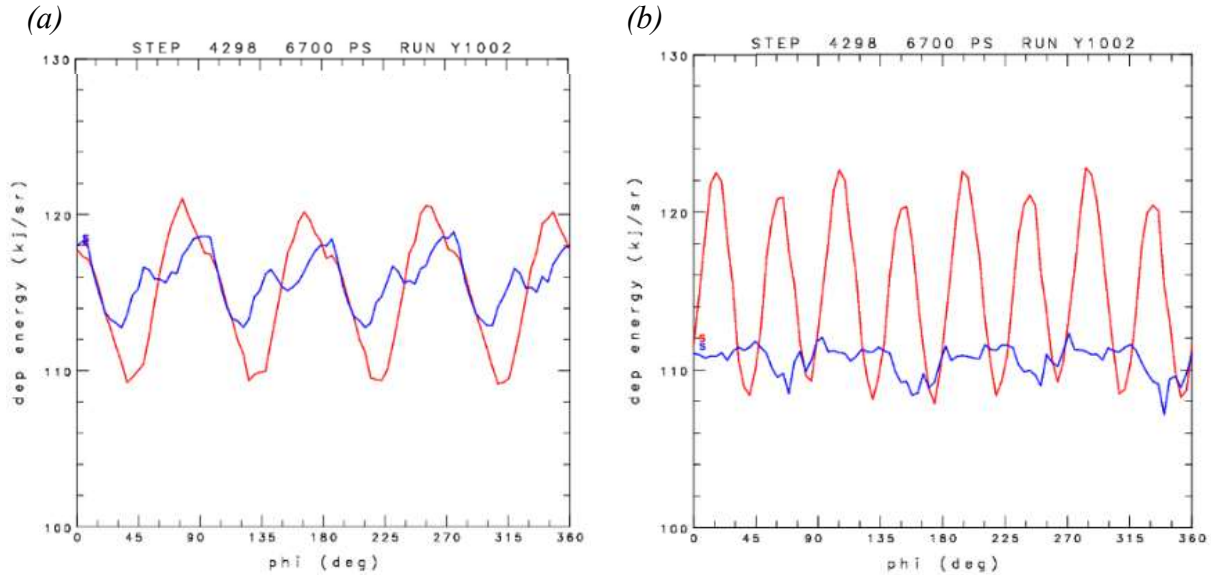


Figure 13. Graphs of deposited energy vs.  $\phi$  at  $\theta=60^\circ$  (a) and  $\theta=50^\circ$  (b) for the previous (red) and optimized (blue) designs. At  $\theta=60^\circ$ , the range of azimuthal variation of the previous design is approximately twice that of the optimized design. At  $\theta=50^\circ$ , the range of azimuthal variation of the previous design is almost five times that of the optimized design.

## 5. Flux Limiter

In the presence of steep temperature gradients, the classical formula for calculating heat flow breaks down, as it predicts heat flow to be grossly overestimated. In its place, a separate formula including the flux limiter,<sup>10</sup> an adjustable constant, is used to more accurately predict the heat flow.

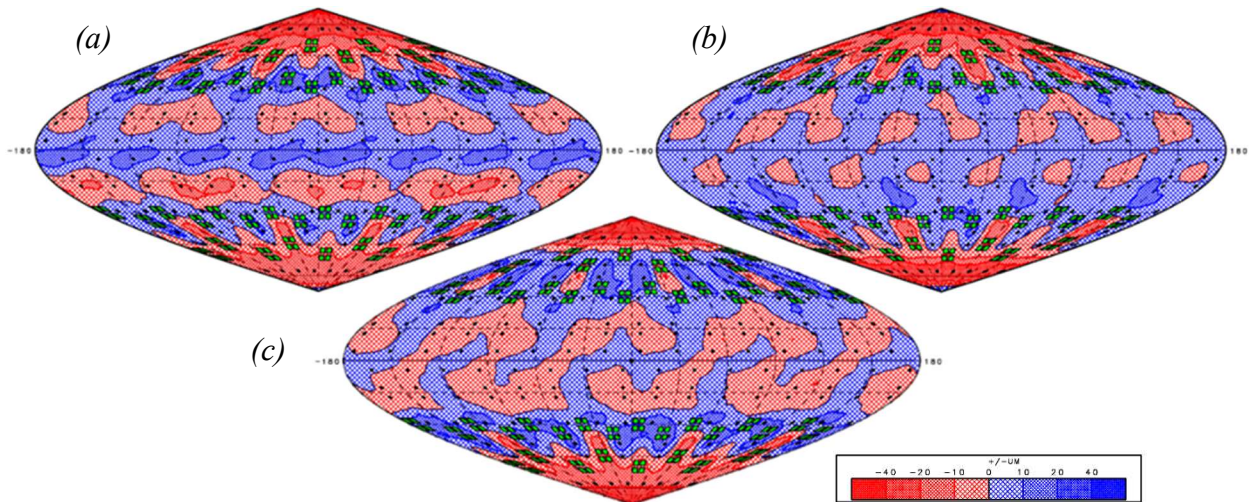


Figure 14. 3D center-of-mass plots at 6.7 ns for varying flux limiters (a) 0.04 (b) 0.08 (c) 0.1. Refer to Figure 12 for the plot of  $f=0.06$ . [Runs 1294, 1312, 1315]

The optimized design used a flux limiter of 0.06, the common value that has been shown to estimate heat flow with the greatest accuracy in many experiments. To investigate the sensitivity of *Revolver* to changes in flux limiter, three additional runs were done, as shown by the 3D center-of-mass plots of the three runs in Figure 14. Even after changing the value of flux limiter, nonuniformity remained almost the same as before.

Table 3 shows that while absorption increases slightly as flux limiter increases, there is no relationship between flux limiter and nonuniformity, as there is no observable pattern in changes of rms nonuniformity as the flux limiter increases. This demonstrates that heat flow within the *Revolver* target is mainly classical, a positive attribute, as its behavior can be predicted with high accuracy using the classical formula.

Flux Limiter (f)	0.04	0.06	0.08	0.1
rms (%)	0.35	0.32	0.32	0.32
rms $\theta$ (%)	0.31	0.27	0.28	0.26
rms $\phi$ (%)	0.16	0.17	0.15	0.19
Absorption (%)	98.3	98.9	99.0	99.1

*Table 3. Rms nonuniformity values across a range of flux limiter values. All rms elements change very little with respect to flux limiter. Within the already low variations in rms, there is no observable pattern in how increasing the flux limiter affects the rms.*

## 6. Too-Large Beam

Although a larger beam spot was absolutely essential in reducing nonuniformity in the azimuthal direction, several problems arise when too large of a beam size is implemented, such as a circular beam with an  $r_0$  of 3000  $\mu\text{m}$  and  $n=4$ . Figure 15 shows the 3D center-of-mass plot at 6.7 ns to illustrate the problem: the equator is greatly undercompressed, resulting in much larger values of radius when  $\theta$  is close to 90 degrees. There is a very clear blue band around the equator of the surface of the target shell, showing a region of extreme undercompression. The poles are much more compressed than the equator, leading the target capsule to be an ellipsoid shape

rather than the desired sphere. The maximum and minimum values are  $+39.5\ \mu\text{m}$  and  $-46.3\ \mu\text{m}$ , respectively.

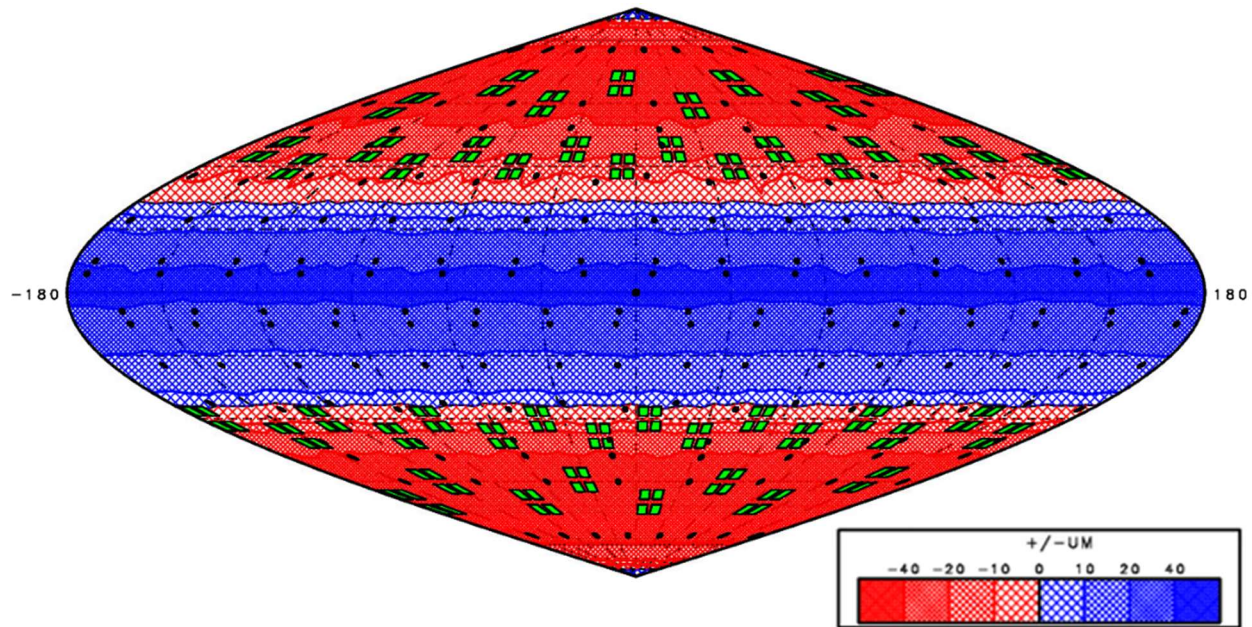
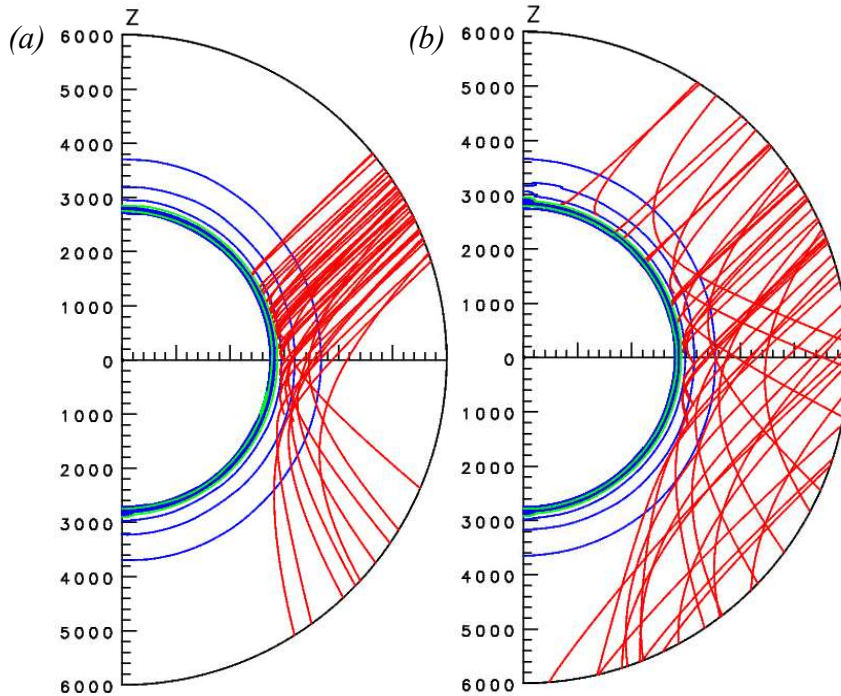


Figure 15. A 3D center-of-mass plot for the design using too-large beams. A distinct blue band is clear across the equator, showing a region of great undercompression. [Run 1003]

An additional problem that's a result of a too-large beam is the large amount of laser energy that misses the target altogether, as shown by the raytrace plots in Figure 16. Figure 16(a) shows the raytrace of the bottom right beam of Ring 4 of the optimized design, where a large portion of the rays hit the target near the equator and are absorbed. Of the deflected rays, almost all of their energy is still deposited in the target. However, the raytrace of the too-large beam [Figure 16(b)] shows that a large portion of the rays from the beam miss the target altogether. Unlike the optimized and previous designs, the rays aren't tightly focused in the vicinity of the equator. The beam size is so large that even though most of the rays are being focused *near* the equator, a lot of rays completely pass by the target without hitting it. The problem with rays that are not significantly deflected is that they can then pass through opposite ports and damage laser optics.



*Figure 16. Raytrace plots showing the optimized design (a) and the too-large beams (b) at 5 ns. The rays of the optimized design are almost all absorbed by the target, with the energy of those deflected still being mostly absorbed. With the too-large beam, a large portion of rays pass straight by the target, potentially damaging laser optics. [Runs 1284, 1003]*

Since a significant portion of the beam's rays pass by the target completely, there is a relatively large amount of transmitted energy from the too-large beam, as shown by Figure 5, which depicts the incident beam energy as well as absorbed (green) and transmitted (red) energies of the too-large beam and the optimized design. While in the optimized design the target absorbs 98.9% of the energy, the too-large beam has an absorption of only 83.2%. The problem arises with the great number of rays completely missing the target from the too-large beam. The large amount of scattered light that comes from the too-large beam, with a maximum value of 215 kJ/sr, compared to a maximum value of scattered light for the optimized design, a mere 9.6 kJ/sr, poses a critical problem that risks damaging the laser optics, since the safety level of scattered light is approximately 60 kJ/sr, as described by Huang.<sup>11</sup>

## 7. Conclusion

By implementing custom phase plates, an optimized design was developed to reduce nonuniformity in the azimuthal direction of *Revolver*. The small, localized regions of over- and

undercompression were eliminated to produce bigger, elliptical beam spots to deposit energy uniformly in the azimuthal direction. Pointings were adjusted, mainly in the  $\theta$  direction, to distribute energy uniformly in the vertical direction. The flux limiter was shown to have little to no effect on the uniformity, suggesting that heat flow in *Revolver* is generally classical. Though a bigger beam size in the horizontal direction was essential to achieving lower nonuniformity in the azimuthal direction, a too-large beam was shown to have inadequate uniformity and problems in the large amount of laser light that passed by the target completely. Custom phase plates improved azimuthal uniformity by more than two-fold and improved the total uniformity as well.

## 8. Acknowledgements

First, I would like to thank my family for their endless support throughout the program and Mr. Bradley Allen for his encouragement of my interest in physics. I'd also like to thank the Laboratory for Laser Energetics for providing myself and my fellow interns the materials and resources necessary for our projects. Finally, I'd like to offer my utmost appreciation to my advisor Dr. R. S. Craxton for his invaluable help and guidance, and for giving us this incredible opportunity.

## 9. References

1. J. Nuckolls, et al., "Laser Compression of Matter to Super-High Densities: Thermonuclear (CTR) Applications," *Nature* **239**, 139 (1972).
2. R. S. Craxton et al., "Direct-Drive Inertial Confinement Fusion: A Review," *Phys. Plasmas* **22**, 110501 (2015).

3. J.D. Lindl, “Development of the Indirect-Drive Approach to Inertial Confinement Fusion and the Target Physics Basis for Ignition and Gain,” *Phys. Plasmas* **2**, 3933 (1995).
4. A. M. Cok, “Development of Polar Direct Drive Designs for Initial NIF Targets,” Laboratory for Laser Energetics High School Research Program (2006).
5. S. Skupsky, et al., “Polar Direct Drive on the National Ignition Facility,” *Phys. Plasmas* **11**, 2763 (2004).
6. K. Molvig et al., “Low Fuel Convergence Path to Direct-Drive Fusion Ignition,” *Phys. Rev. Lett.* **116**, 255003 (2016).
7. E. M. Garcia, private communication.
8. P.W. McKenty et al., “Evaluation of the Revolver Ignition Design at the National Ignition Facility Using Polar-Direct-Drive Illumination,” presented at the 59th Annual Meeting of the American Physical Society Division of Plasma Physics, Paper N07-5, October 2017.
9. L. Tucker, “A Design for a Shock Ignition Experiment on the NIF Including 3-D Effects,” Laboratory for Laser Energetics High School Research Program (2011).
10. R.C. Malone, et al., “Indications of Strongly Flux-Limited Electron Thermal Conduction in Laser-Target Experiments,” *Phys. Rev. Lett.* **34**, 721 (1975).
11. P. Huang, “Analysis of Unabsorbed Light from Exploding-Pusher Targets Used for Proton Backlighting on the National Ignition Facility,” Laboratory for Laser Energetics High School Research Program (2015).